J. Fluid Mech. (2007), *vol.* 574, *pp.* 449–463.
doi:10.1017/S0022112006004253 Printed in the United Kingdom

Boundary layer flow and bed shear stress under a solitary wave

PHILIP L.-F. LIU, YONG SUNG PARK AND EDWIN A. COWEN

School of Civil and Environmental Engineering, Cornell University, Ithaca, NY 14853, USA

(Received 19 January 2006 and in revised form 28 August 2006)

Liu & Orfila (*J. Fluid Mech.* vol. 520, 2004, p. 83) derived analytical solutions for viscous boundary layer flows under transient long waves. Their analytical solutions were obtained with the assumption that the nonlinear inertia force was negligible in the momentum equations. In this paper, using Liu & Orfila's solution and the solutions for the nonlinear boundary layer equations, we examine the boundary layer flow characteristics under a solitary wave. It is found that while the horizontal component of the free-stream velocity outside the boundary layer always moves in the direction of wave propagation, the fluid particle velocity near the bottom inside the boundary layer reverses direction as the wave decelerates. Consequently, the bed shear stress also changes sign during the deceleration phase. Laboratory measurements, including the free-surface displacement, particle image velocimetry (PIV) resolved velocity fields of the viscous boundary layer, and the calculated bed shear stress were also collected to check the theoretical results. Excellent agreement is observed.

1. Introduction

The theoretical treatment of the effects of viscous damping on solitary waves was first presented by Keulegan (1948). Mei (1983) rederived Keulegan's results by the perturbation method of Ott & Sudan (1970). Using a Fourier transform method, Keulegan also obtained the solution for the horizontal velocity in the bottom boundary layer in an integral form. Since the primary interest of their work was the estimation of damping rate, neither Keulegan nor Mei examined the structure of the boundary layer velocity field or the bed shear stress. More recently, in an effort to include the bottom boundary layer effects in Boussinesq-type (depth-integrated wave) equations, Liu & Orfila (2004, hereafter LO) obtained analytical solutions for viscous boundary layer flows under arbitrary transient long waves. Using their new formulation, LO also calculated the damping rate for the solitary wave, which agreed with that derived by Keulegan. The analytical formula for the damping rate has been verified with the measurements of Russell (1838) and Liu *et al.* (2006).

Besides the damping rate, the bed shear stress also plays an important role in near-bed processes. However, direct measurements of bed shear stress are difficult and scarce. Ippen & Mitchell (1957) used a shear plate and measured the time histories of bottom shear stress under solitary waves. Since a shear plate is an intrusive device and the measurement area is quite large, the quality of their data is not very high. Nevertheless, the measurements reveal that the bed shear stress changes sign as the solitary wave passes the measurement area. In other words, the bed shear stress is not in phase with the free-stream velocity above the bottom boundary layer. Using a

hot-film probe, Jensen, Sumer & Fredsoe (1989) measured the bed shear stress on a smooth bed under oscillatory flows in their U-tube experiments. Although the accuracy of the hot-film probe was not discussed, Jensen *et al.* (1989) clearly demonstrated the phase lag between the bed shear stress and the free-stream velocity for different Reynolds numbers. This feature has significant implications for the modelling of sediment transport and morphological changes and deserves more careful investigation.

In recent years, laser Doppler velocimeters (LDV) have been used in several oscillatory boundary layer experiments, investigating the transition from laminar to turbulent flow on a smooth bed, the turbulent boundary layer over a rough bed (e.g. Sleath 1987; Jensen *et al.* 1989), and the mass transport velocity inside the boundary layer over a permeable bottom (Liu, Davis & Downing 1996). The LDV technique is non-intrusive and provides the time history of velocity at a fixed point. The velocity profile inside a boundary layer is obtained by moving the LDV through the boundary layer. The bed shear stress can then be inferred from the velocity profile. While the necessary resolution to directly calculate the fluid stress from single-point velocity data is achievable, it is in general necessary to measure each spatial location in a new realization of the experiment, which leads to additional uncertainty in the measurement of stress relative to calculations from synoptic measurement techniques (e.g. techniques that capture the information necessary to determine the gradient within a single realization of the experiment).

An alternative to the LDV technique is particle image velocimetry (PIV), a whole-field measurement technique. The PIV technique has been successfully employed in a wide variety of flows such as the measurement of the vorticity field in the vicinity of an object subject to either a steady current or an oscillatory flow (Lin & Rockwell 1994, 1995). Chang & Liu (1998, 1999) have also reported PIV measurements of velocity and vorticity fields under breaking waves. Cowen & Monismith (1997) demonstrated the ability of PIV to resolve steady boundary layers and Cowen *et al.* (2003) successfully measured the time-dependent boundary layer in the swash zone on a planar glass beach. Liu, Al-Banna & Cowen (2004) measured the velocity and turbulent characteristics in a turbulent boundary layer over a ripple bed.

The objective of this paper is to investigate theoretically and experimentally the characteristics of the laminar bottom boundary layer under a solitary wave. The theoretical framework is based on LO's perturbation analysis. However, we extend their linear boundary layer solution, which is in a closed form, to fully nonlinear boundary layer solutions that must be solved numerically. We present a set of PIV-based experimental data measuring the time history of velocity profiles inside the bottom boundary layer. The boundary layer thickness in our experiments is of the order of 1 mm. The vertical resolution of our PIV data is 0.04 mm, allowing us to estimate the bed shear stress by taking the vertical gradient of the horizontal velocity at the bed. Experimental data for the velocity and bottom shear stress are used to verify the theoretical results. Excellent agreement is observed. The theoretical solutions are employed to further examine the importance of nonlinearity in the boundary layer flow and mass transport under solitary waves.

2. Governing equations and boundary conditions for boundary layer flow

Following LO's approach we consider a solitary wave with the surface displacement $\zeta'(x', t')$ propagating in a constant water depth, h'. The solitary wave is characterized by the wave height, H_0', a horizontal length scale, l_o', which is related to the width

of the solitary wave shape, and the time scale, $l'_o/\sqrt{g'h'}$. The following dimensionless variables are introduced:

$$\left.\begin{aligned} &x = x'/l'_o, \quad z = z'/h', \quad t = \sqrt{g'h'}t'/l'_o, \\ &\zeta = \zeta'/H'_0, \quad p = p'/\rho' g' H'_0, \\ &u = u'/\epsilon\sqrt{g'h'}, \quad w = \mu w'/\epsilon\sqrt{g'h'}, \end{aligned}\right\} \tag{2.1}$$

in which p' denotes the pressure, u' the horizontal velocity component in the x'-direction, w' the vertical velocity component in the z'-direction, ρ' the fluid density, and g' the gravitational acceleration. Two dimensionless parameters have been introduced in the above equations:

$$\epsilon = H'_0/h', \quad \mu = h'/l'_o. \tag{2.2}$$

The flow motions associated with solitary waves can be considered as essentially irrotational except in the boundary layers adjacent to the free surface, $z = \epsilon\zeta$, and the bottom, $z = -1$. Inside these boundary layers, the fluid viscosity plays the role of generating and diffusing vorticity into the flow domain. Therefore, rotational velocity components must be added inside the boundary layers. Since the no-slip boundary condition on the bottom is required, the leading-order horizontal rotational velocity component inside the bottom boundary layer must be the same as that of the irrotational velocity, i.e. $O(1)$. On the other hand, on the free surface, only the shear-stress-free condition is required. The leading-order horizontal rotational velocity component inside the free-surface boundary layer is weaker, i.e. $O(\alpha)$ (Mei & Liu 1973), where

$$\alpha^2 = \frac{\nu'}{l'_o\sqrt{g'h'}}, \tag{2.3}$$

with ν' being the kinematic viscosity of the fluid, and α^2 can be viewed as an inverse of Reynolds number. More importantly, the boundary layer thickness is $O(\alpha)$. Consequently, in this paper we shall only focus on bottom boundary layer flows.

2.1. *Analytical solutions for solitary waves*

When the viscous effect is completely ignored, analytical solutions describing a solitary wave are available. For example, Grimshaw (1971) presented the solution for the free-surface displacement up to $O(\epsilon^2)$ as follows:

$$\zeta = s^2 - \frac{3}{4}\epsilon s^2 q^2 + \epsilon^2\left(\frac{5}{8}s^2q^2 - \frac{101}{80}s^4q^2\right), \tag{2.4}$$

where

$$s = \operatorname{sech}\left[\frac{\beta}{\mu}(x - Ct)\right], \tag{2.5}$$

$$q = \tanh\left[\frac{\beta}{\mu}(x - Ct)\right], \tag{2.6}$$

$$\beta = \sqrt{\frac{3\epsilon}{4}}\left(1 - \frac{5}{8}\epsilon + \frac{71}{128}\epsilon^2\right), \tag{2.7}$$

$$C = \sqrt{1 + \epsilon - \frac{1}{20}\epsilon^2 - \frac{3}{70}\epsilon^3}. \tag{2.8}$$

The corresponding horizontal and vertical velocity can be expressed as

$$u(x,z,t)=\frac{\partial \Phi}{\partial x}=s^2-\epsilon\left[-\frac{1}{4}s^2+s^4+(z+1)^2\left(\frac{3}{2}s^2-\frac{9}{4}s^4\right)\right]$$
$$-\epsilon^2\left[\frac{19}{40}s^2+\frac{1}{5}s^4-\frac{6}{5}s^6+(z+1)^2\left(-\frac{3}{2}s^2-\frac{15}{4}s^4+\frac{15}{2}s^6\right)\right.$$
$$\left.+(z+1)^4\left(-\frac{3}{8}s^2+\frac{45}{16}s^4-\frac{45}{16}s^6\right)\right], \tag{2.9}$$

$$w(x,z,t)=\frac{\partial \Phi}{\partial z}=\sqrt{\frac{3\mu^2}{\epsilon}}(z+1)q\left\{-\epsilon s^2+\epsilon^2\left[\frac{3}{8}s^2+2s^4+(z+1)^2\left(\frac{1}{2}s^2-\frac{3}{2}s^4\right)\right]\right.$$
$$+\epsilon^3\left[\frac{49}{640}s^2-\frac{17}{20}s^4-\frac{18}{5}s^6+(z+1)^2\left(-\frac{13}{16}s^2-\frac{25}{16}s^4+\frac{15}{2}s^6\right)\right.$$
$$\left.\left.+(z+1)^4\left(-\frac{3}{40}s^2+\frac{9}{8}s^4-\frac{27}{16}s^6\right)\right]\right\}. \tag{2.10}$$

We remark here that the velocity potential Φ has been introduced for the irrotational velocity component. The leading-order, $O(1)$, solutions of Grimshaw's formulae will be called Boussinesq solutions for solitary waves.

2.2. *Bottom boundary layer analysis*

Following LO's analysis, we now introduce the following perturbation expansions for the velocity field in the bottom boundary layer:

$$u=\frac{\partial \Phi}{\partial x}(x,z,t)+u_0^r(x,z,t)+\alpha u_1^r(x,z,t)+\cdots, \tag{2.11}$$

$$w=\frac{\partial \Phi}{\partial z}+\alpha\mu w_1^r+\cdots. \tag{2.12}$$

The perturbation expansions are accurate to $O(\alpha)$. In this paper, we shall assume that the leading-order irrotational horizontal velocity for a solitary wave is given by (2.9) and shall focus on the solution for the rotational velocity component inside the bottom boundary layer. Since the ratio of the boundary layer thickness and the length scale is $O(\alpha)$, we introduce the stretched coordinate

$$\eta=\frac{z+1}{\alpha/\mu}. \tag{2.13}$$

The leading-order continuity equation and the horizontal momentum equation for the rotational velocity in the bottom boundary layer become

$$\frac{\partial u_0^r}{\partial x}+\frac{\partial w_1^r}{\partial \eta}=0, \tag{2.14}$$

$$\frac{\partial u_0^r}{\partial t}+\epsilon\left[u_0^r\frac{\partial u_0^r}{\partial x}+w_1^r\frac{\partial u_0^r}{\partial \eta}\right]=\frac{\partial^2 u_0^r}{\partial \eta^2}. \tag{2.15}$$

The leading-order dynamic pressure gradient inside the boundary layer is $\partial p/\partial \eta = O(\alpha\mu)$.

The no-slip and no-flux boundary conditions on the bottom require that the rotational velocity satisfies the following boundary conditions:

$$u_0^r=-\frac{\partial \Phi}{\partial x},\quad \frac{\partial \Phi}{\partial z}=-\alpha\mu w_1^r,\quad \eta=0. \tag{2.16}$$

At the outer edge of the boundary layer, $\eta \to \infty$, the horizontal rotational velocity components vanish,

$$u_0^r, \quad w_1^r \to 0, \quad \eta \to \infty. \tag{2.17}$$

2.2.1. *Linearized boundary layer solutions*

To find the boundary layer solution for a general transient wave, LO linearized the boundary layer equation, (2.15):

$$\frac{\partial u_0^r}{\partial t} = \frac{\partial^2 u_0^r}{\partial \eta^2}, \tag{2.18}$$

and found the analytical solution as

$$u_0^r(x, \eta, t) = -\frac{\eta}{\sqrt{4\pi}} \int_0^t \frac{\partial \Phi(x, z=-1, \tau)/\partial x}{\sqrt{(t-\tau)^3}} e^{-\eta^2/4(t-\tau)} \, d\tau. \tag{2.19}$$

From the continuity equation, (2.14), the vertical rotational velocity component can be obtained by integration,

$$w_1^r(x, \eta, t) = -\int_\eta^\infty d\overline{\eta} \frac{\overline{\eta}}{2\sqrt{\pi}} \int_0^t \frac{\partial^2 \Phi(x, z=-1, \tau)/\partial x^2}{\sqrt{(t-\tau)^3}} e^{-\overline{\eta}^2/4(t-\tau)} \, d\tau. \tag{2.20}$$

LO also showed that the leading-order bottom shear stress at $\eta = 0$ can be expressed as:

$$\tau_b = \left. \frac{\partial u_0^r}{\partial \eta} \right|_{\eta=0} = \frac{1}{\sqrt{\pi}} \int_0^t \frac{\partial^2 \Phi(x, z=-1, \tau)/\partial x \partial \tau}{\sqrt{t-\tau}} \, d\tau, \tag{2.21}$$

in which the irrotational velocity has been assumed to be zero initially.

Substitution of (2.9) into (2.19) yields the horizontal rotational velocity component under a solitary wave. For convenience, we introduce a moving coordinate, $\xi = x - Ct$, where C is the phase speed of the wave as given in (2.8). If x is set equal zero, $-\xi = Ct$ acts like time. In figure 1, the time histories of the rotational velocity component, the irrotational velocity component, and the total velocity inside the boundary layer are plotted for $\epsilon = 0.2$ at several elevations $\eta = 0, 0.25, 1.0, 10.0$, respectively. It is clear that the irrotational velocity remains positive (in the same direction as wave propagation) and the rotational velocity component takes an opposite sign. Since the no-slip condition is required at the bottom, the rotational velocity is the mirror image (with an opposite sign) of the irrotational velocity component. Therefore, positive vorticity is generated from the bottom as fluid particles outside the boundary layer accelerate towards the wave crest. Once the fluid flow outside the boundary layer reaches the maximum speed and starts to decelerate, negative vorticity is generated from the bottom. Both positive vorticity (during the acceleration phase) and negative vorticity (during the deceleration phase) are diffused from the bottom into the boundary layer through viscous diffusion. Therefore, the maximum (negative) value of the rotational velocity component lags behind the maximum (positive) irrotational velocity, resulting in reverse flow near the bottom during the deceleration phase. Obviously the boundary layer velocity depends on the input data for the irrotational velocity component. In figure 1 we also plot the time histories of the boundary layer

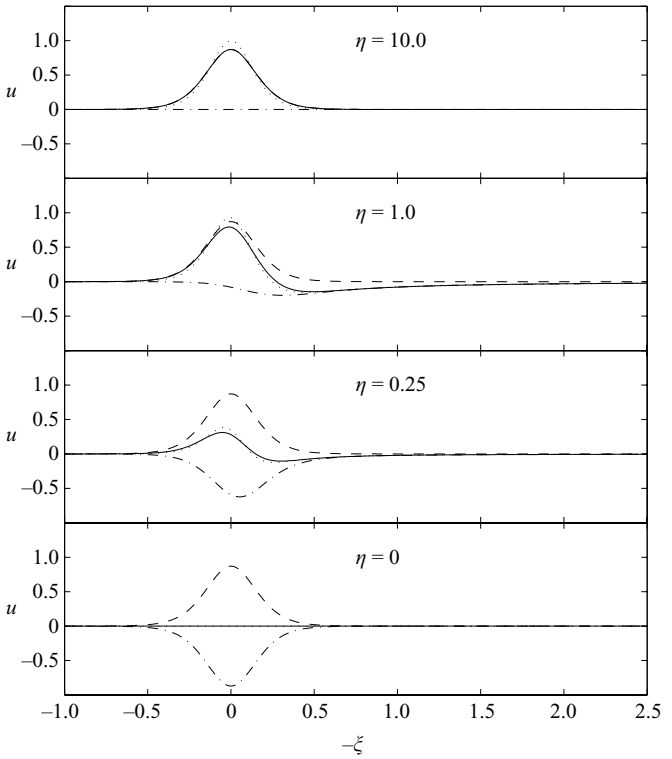

FIGURE 1. Horizontal dimensionless velocity components at different elevations inside the boundary layer: – – – –, the irrotational velocity component (Grimshaw's solutions); —·—, the rotational velocity component; ——, the total velocity using Grimshaw's solutions; ·····, the total velocity using Boussinesq's solutions.

velocity using the Boussinesq solutions as the irrotational velocity components, which are slightly larger than those determined from Grimshaw's solutions.

The bottom shear stress can be calculated directly from (2.21) using (2.9) as the input irrotational velocity. The results for $\epsilon = 0.1, 0.2, 0.5$ are shown in figure 2. Because of the flow reversal near the bottom, the bed shear stress also changes sign; the shear stress becomes negative when the flow starts to decelerate.

2.2.2. *Nonlinear boundary layer solutions*

If the nonlinear inertia term is not negligible, the full boundary layer equation (2.15) must be solved numerically. Using the moving coordinate, $\xi = x - Ct$, the boundary layer equation, (2.15), becomes

$$\left(\epsilon u_0^r - C\right) \frac{\partial u_0^r}{\partial \xi} - \left(\epsilon \int_\eta^\infty \frac{\partial u_0^r}{\partial \xi}\, \mathrm{d}\eta'\right) \frac{\partial u_0^r}{\partial \eta} = \frac{\partial^2 u_0^r}{\partial \eta^2}. \tag{2.22}$$

One could try to solve the above differential-integral equation for u_0^r. Here, we propose to approximate it by approximating the integrand of the integral by the leading-order term, i.e.

$$\frac{\partial u_0^r}{\partial \xi} = -\frac{1}{C} \frac{\partial^2 u_0^r}{\partial \eta^2} + O(\epsilon).$$

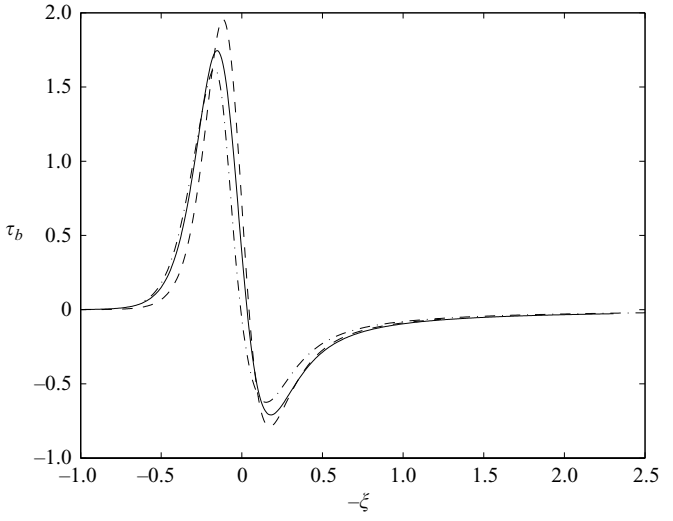

FIGURE 2. Dimensionless bed shear stress, (2.21), for different values of nonlinearity: – – – –, $\epsilon = 0.1$; ——, $\epsilon = 0.2$; — · —, $\epsilon = 0.5$.

Thus, the approximate nonlinear boundary layer equation becomes

$$\epsilon u_0^r \frac{\partial u_0^r}{\partial \xi} - C \frac{\partial u_0^r}{\partial \xi} - \frac{\epsilon}{C} \left(\frac{\partial u_0^r}{\partial \eta} \right)^2 = \frac{\partial^2 u_0^r}{\partial \eta^2} + O(\epsilon^2). \tag{2.23}$$

The boundary conditions are rewritten in terms of the moving coordinate as

$$u_0^r = -\frac{\partial \Phi}{\partial x}, \quad \eta = 0, \tag{2.24}$$

and

$$u_0^r \to 0, \quad \eta \to \infty. \tag{2.25}$$

The approximate nonlinear boundary layer equation (2.23) is solved numerically by an iterative scheme, in which the nonlinear terms are calculated based on the results from the previous iteration, while the linear operator is discretized by the Crank–Nicholson method. Using the linear solution as an initial guess, the iteration continues until the maximum relative error between the current and the previous iteration results is smaller than 10^{-6}. The analysis reveals that the nonlinear effects are not very significant, and converged solutions are obtained within a very small number of iterations (usually, less than ten). In figure 3 the solutions for both the linear and nonlinear boundary layer equations are shown together. The irrotational velocity is Grimshaw's higher-order solution, (2.9), with $\epsilon = 0.5$. The solutions based on the linear and nonlinear equations are surprisingly close. There are two nonlinear terms in the nonlinear boundary layer equation, i.e. the first and third terms on the left-hand side of (2.23). The values of these two terms at $\eta = 0.1$ are shown in figure 4. Figure 4(*a*) shows that when the linear boundary layer equation is solved, the results of the linear terms are indeed identical as expected. In (*a*) we also plot the computed values of the nonlinear terms by using the linear solutions. These values are small, but not entirely negligible. In figure 4(*b*) the results for all four terms in the nonlinear boundary layer equation are plotted when the nonlinear equation is solved. It is interesting to observe that the values for the time-derivative-like linear term (the linear term on the left-hand side of (2.23)) and the values for the nonlinear terms

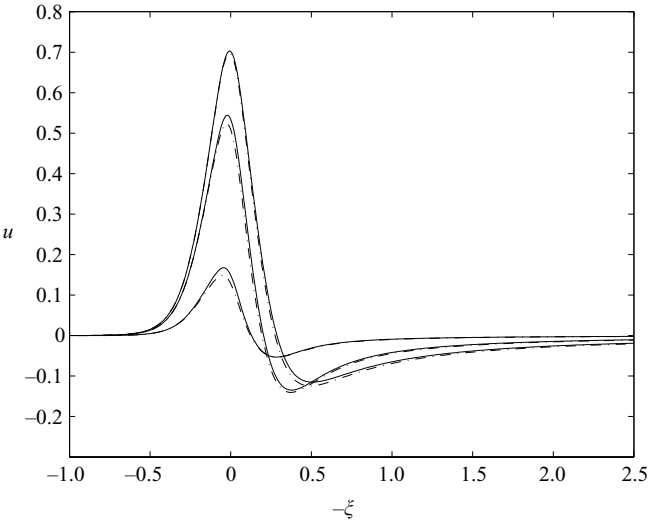

FIGURE 3. Time histories of dimensionless horizontal velocities at $\eta = 0.1$, 0.5, and, 1.0 (bottom to top) for $\epsilon = 0.5$: ——, the solutions of the nonlinear boundary layer equation; — · —, the solutions of the linear boundary layer equation.

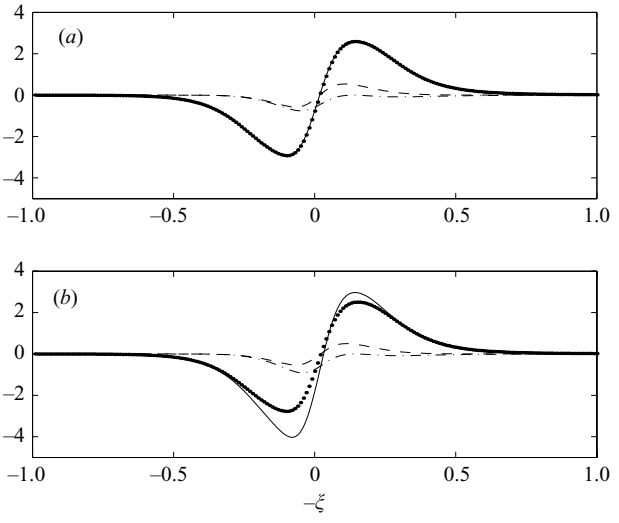

FIGURE 4. Comparisons between linear and nonlinear terms calculated from (*a*) the linear solutions and (*b*) the nonlinear solutions: ●●●, the linear term on the left-hand side of (2.23); – – – – –, the first nonlinear term of (2.23); — · —, the second nonlinear term of (2.23); ——, the linear term on the right-hand side of (2.23).

remain more or less the same as those shown in (*a*) (i.e. from the linear solutions). The only significant changes appear in the diffusion term on the right-hand side of the nonlinear equation.

3. Experiments

To validate the theories presented in the previous section, a set of laboratory experiments measuring the boundary layer velocities under solitary waves was carried out in the DeFrees Hydraulics Laboratory at Cornell University.

Wave height H_0' (cm)	Wavelength l_0' (m)	Wave period T' (s)	ϵ	μ	α
0.8	2.29	2.20	0.08	0.0437	0.0006
2.0	1.52	1.37	0.2	0.0658	0.0008
3.0	1.23	1.05	0.3	0.0813	0.0009

TABLE 1. Characteristics of the solitary waves generated in the experiments.

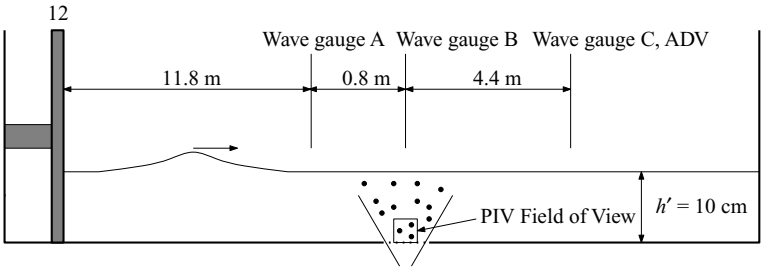

FIGURE 5. A sketch of the experimental set-up.

3.1. *Experimental set-up*

The experiments were conducted in a wave tank (32 m long, 0.6 m wide, and 0.9 m deep), which is equipped with a piston-type wavemaker. The tank has glass sidewalls and a painted steel bottom. One section of the tank is equipped with a clear extruded acrylic bottom allowing the delivery of laser light from below.

Three different solitary waves have been studied by changing the wave heights (0.8, 2.0 and 3.0 cm), while the water depth is kept constant, $h' = 10$ cm. The solitary waves were generated using Goring's theory (Goring 1978) with the wavelength cutoff corresponding to a surface displacement of 1.0 % of the wave height. The characteristics of the waves generated in the experiments are summarized in table 1. Three acoustic wave gauges (Banner Engineering SI8U) and an ADV (Nortek Vectrino with Plus Firmware) were used along with our in-house PIV system. The locations of measurements are shown in figure 5. The PIV system is used primarily to measure the velocity field in the bottom boundary layer. PIV measurements were carried out in the region with the acrylic bottom and the laser light sheet was delivered vertically through the bed.

Figure 6 shows the surface profile measured at wave gauge B sampled at 100 Hz (above the centre of the PIV measurement region) for the case where wave height is 2.0 cm ($\epsilon = 0.2$). Grimshaw's higher-order solution, (2.4), is also plotted in the same figure. The agreement between the theoretical results and experimental data is excellent. Similar excellent agreement is also observed for the other two wave conditions, i.e. $\epsilon = 0.08$ and 0.3.

As indicated in figure 5, ADV data were also collected 4.4 m downstream from the PIV measurement location and 2 cm above the bottom. The sampling frequency is 40 Hz and measurement volume is a circular cylinder with 6 mm diameter and 7 mm height. The experimental data for the horizontal velocity component agree very well with the theoretical solution, (2.9) (see figure 7). On the other hand, discrepancies between the experimental data for the vertical velocity and the theoretical result, (2.10), are visible. However, the expected trend is clearly captured by the ADV data and the amplitudes agree to well within the uncertainty of the measurement. We remark here

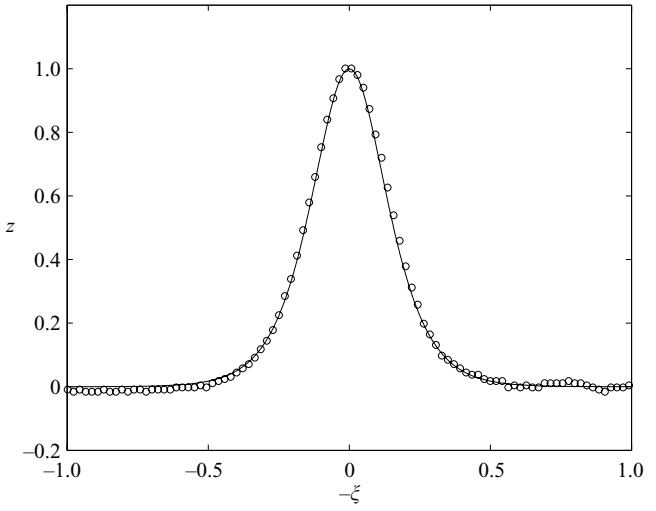

FIGURE 6. Theoretical and experimental dimensionless water surface profiles for $\epsilon = 0.2$: ——, Grimshaw's solutions; ○, the experimental data.

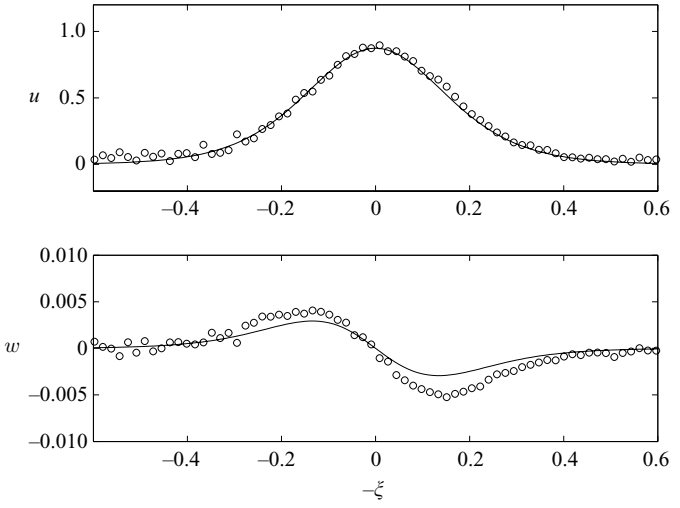

FIGURE 7. Theoretical and experimental dimensionless water particle velocities in the irrotational region for $\epsilon = 0.2$: ——, Grimshaw's solution; ○, experimental data.

that close examination of the vertical rotational velocity component, (2.20), reveals that its contribution to the total vertical velocity, (2.12), at the ADV measurement location is too small to explain the discrepancies shown in figure 7. Again, similar very good agreement between the ADV data and the theoretical predictions is observed for the other two cases.

3.2. *PIV analysis procedure*

The primary objective of our experiments was to measure the velocity field inside the bottom boundary layer under the solitary wave. The resolution of the measurements must be sufficient that the bottom shear stress can be accurately calculated.

The field of view (FOV) of the image area was illuminated with a Spectra Physics PIV400-30 Nd:YAG laser system (300 mJ/pulse, 60 Hz dual head system). By passing

the laser beam through a cylindrical lens, a light sheet was formed, which was delivered from below the tank bottom to avoid disturbances from the free surface. The FOV was set parallel to the sidewalls and slightly off the tank centreline to increase image magnification (and thereby decrease the FOV). The FOV was 15 cm from the nearest sidewall and the effects of the sidewall boundary layer are not significant. For all of the experimental cases, the image acquisition system was triggered to capture image pairs for subsequent cross-correlation analysis with a 2.00 ms time delay. Images were collected with an SMD 1m60-20 camera (12 bits/pixel, 60 Hz, 1024×1024 pixel) at 30 Hz, yielding a velocity field rate of 15 Hz. A cylindrical lens (TSI) with focal length $f = -50.0$ mm was used and the square FOV had side length 20 mm. A more detailed description of the PIV technique can be found in Cowen & Monismith (1997) and Cowen *et al.* (2003). Cowen & Monismith (1997) suggested optimal values for several parameters so as to obtain high-quality PIV data; these criteria were met in our experiments.

Following Cowen & Monismith (1997), the images are preprocessed by removing the global minimum value across the image sets (180 images per experiment). This significantly reduces the effects of glare at the bed and allows excellent displacement measurements right up to the bed. While Δt was set at 2.00 ms to minimize the effects of shear, it was recognized that shear would be a significant issue in the boundary layer. Further, since the goal is to make highly accurate and resolved measurements to allow the direct determination of the gradient, a rectangular interrogation subwindow with long dimension in the horizontal was utilized (128×8 pixel with 75 % overlap), which yielded 29 subwindows in the horizontal, 487 in the vertical (0.6 mm horizontal and 0.04 mm vertical resolution). This allows long displacements in the horizontal to be resolved while minimizing the negative impacts on the correlation due to vertical gradients.

Spurious vectors were flagged using an adaptive Gaussian window filter where all returned velocities at a given elevation above the bed are assumed to be homogeneous. The procedure is as follows. First, based on the sample size (initially, $N = 29$ in each row), statistics are calculated to set a threshold, beyond which vectors are removed. Then statistics are recalculated until there is convergence. This filter rejected 20 % of the returned data. However, more than 11 000 data points remain. No attempt is made to smooth or interpolate the original data at this point.

4. Experimental measurements and theoretical results

The vertical profiles of the horizontal velocity inside the boundary layer for $\epsilon = 0.2$ are shown in figures 8 and 9 at different phases. Since the difference between the linear boundary layer solutions and the nonlinear solutions is very small, only the nonlinear solutions are plotted. In figure 8 the flow at the outer edge of the boundary layer is accelerating and reaches the maximum value under the wave crest. During the accelerating phase, the horizontal velocities inside the boundary layer are moving in the same direction as wave propagation. On the other hand, as the wave crest passes the measurement location, the velocity starts to decrease. Consequently, the horizontal velocity reverses its direction starting from the bottom and diffuses upward into the entire boundary layer. In plotting the PIV data horizontal homogeneity is assumed and the PIV data are averaged along the wave propagation direction within the FOV. In figure 10 the time history of the horizontal velocity at $\eta = 0.5$ for $\epsilon = 0.2$ is shown. The flow reversal is clearly demonstrated. Excellent agreement of the experimental data with the theoretical solutions is observed.

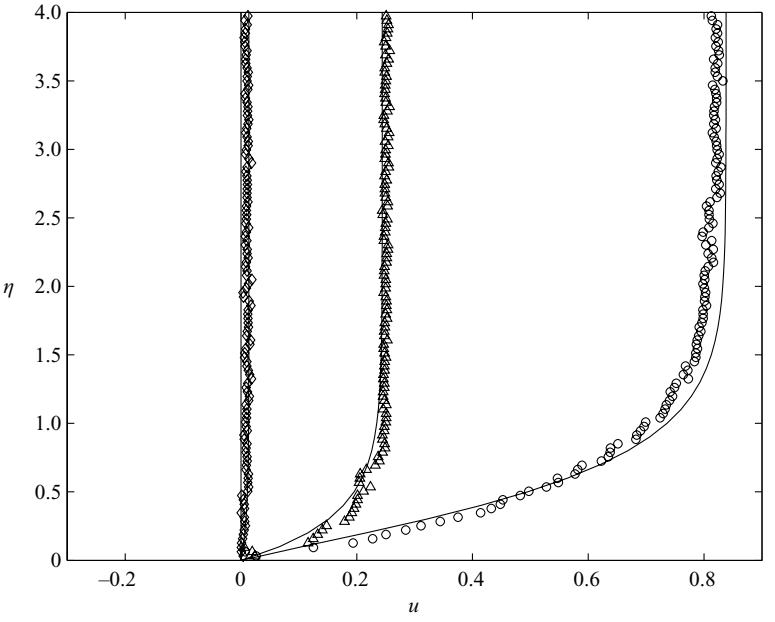

FIGURE 8. Vertical profiles of the dimensionless horizontal velocity during the accelerating phase for $\epsilon = 0.2$: ——, the numerical solutions of the nonlinear boundary equation. Experimental data are denoted as follows: ⋄, $\xi = 0.50$; △, $\xi = 0.22$; ○, $\xi = -0.06$.

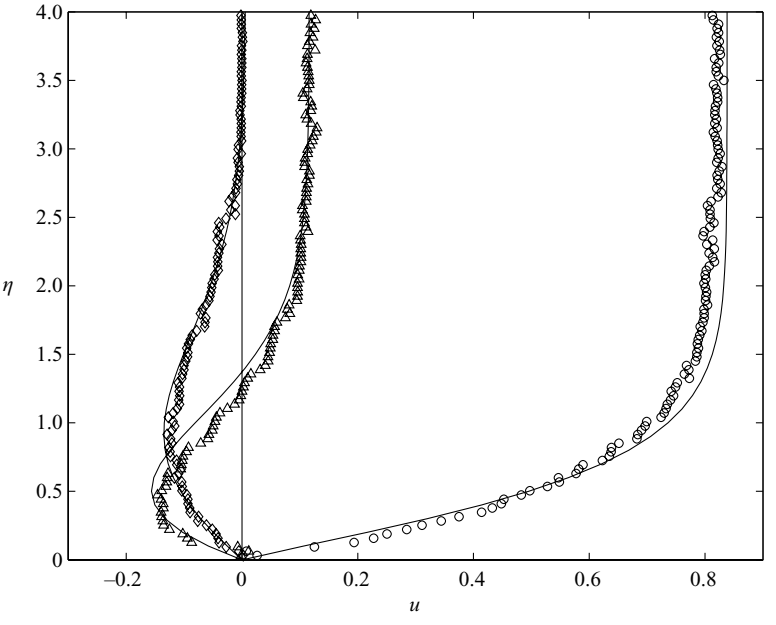

FIGURE 9. Vertical profiles of the horizontal dimensionless velocity during the decelerating phase for $\epsilon = 0.2$: ——, the numerical solutions of the nonlinear boundary equation. Experimental data are denoted as follows: ⋄, $\xi = -0.63$; △, $\xi = -0.34$; ○, $\xi = -0.06$.

As mentioned before, one of the significant consequences of the flow reversal, caused by flow deceleration, is that the bottom shear stress changes direction. In other words,the bottom shear stress is 180° out of phase with the free-stream velocity,

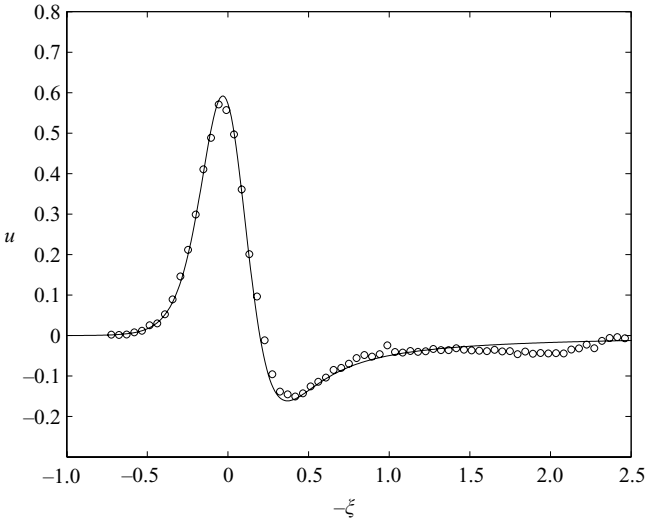

FIGURE 10. Time history of the horizontal dimensionless velocity at $\eta = 0.5$ for $\epsilon = 0.2$: ——, the nonlinear solutions; ○, the experimental data.

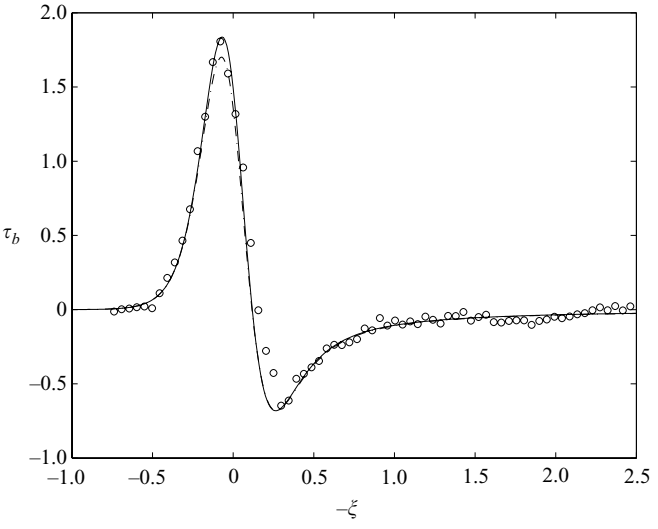

FIGURE 11. Time history of the dimensionless bottom shear stress for $\epsilon = 0.2$: ——, the nonlinear solutions; — · —, the linear solutions (2.21); ○, the experimental data.

defined as the horizontal velocity at the outer edge of the boundary layer. The theoretical predictions are compared with estimates from PIV data near the bottom (see figure 11). The experimental results are obtained by least-square fitting a straight line through eight data points (within 0.3 mm) above the bed. The peak value of the bed shear stress calculated from the nonlinear theory is slightly higher than that from the linear solution (2.21). Excellent agreement of the experimental data with the theoretical solutions is observed.

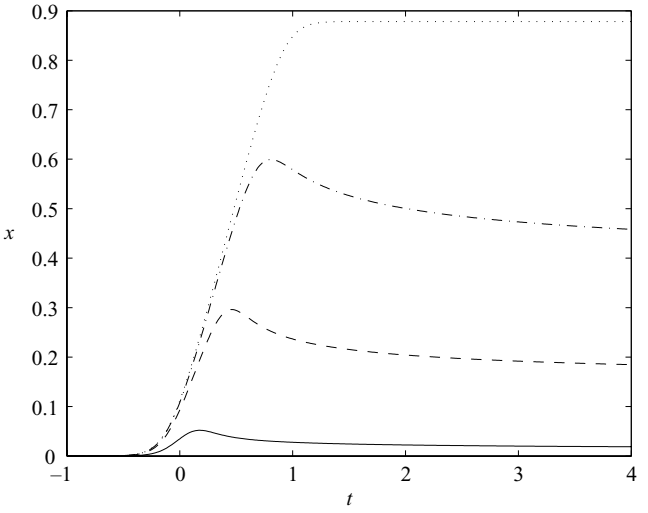

FIGURE 12. Net horizontal dimensionless displacements of particles initially located at four different vertical positions for $\epsilon = 0.2$: ——, $\eta = 0.1$; – – – –, $\eta = 0.5$; —·—, $\eta = 1.0$; ·····, $\eta = 10.0$.

5. Mass transport inside the boundary layer

With the identification of the reverse flow within the boundary layer a natural question arises regarding the resultant net displacement profile of water parcels. The displacement of water parcels can be expressed as an integral equation:

$$x(t) = x_0 + \int_{t_0}^{t} u(x(\tau), \tau)\, \mathrm{d}\tau, \tag{5.1}$$

where all quantities are suitably non-dimensionalized. Assuming that the vertical velocity component is negligible, net displacements at four different vertical positions have been calculated using the fourth-order Runge–Kutta method.

As we can see in figure 12, the net displacements are always positive. That is, even though the reverse flow occurs, it is not strong enough to cause a net negative displacement at any elevation within the boundary layer.

6. Concluding remarks

In this paper we have examined the laminar bottom boundary layer flows under a solitary wave both theoretically and experimentally. The following conclusions can be drawn:

1. The horizontal velocity inside the boundary layer is not always in phase with the free-stream velocity. A flow reversal starts at the bed as the flow at the outer edge of the boundary layer begins to decelerate.

2. Numerical results for the nonlinear boundary layer equation indicate that the nonlinear advection terms have a weak impact on the solutions even for a relatively large solitary wave.

3. The bottom shear stress changes sign as the near-bed velocity reverses its direction.

4. The PIV method is shown to be an accurate measurement technique to measure the boundary layer velocity and the bed shear stress.

Recently LO's boundary layer analysis was extended to turbulent boundary layer flows by Liu (2006), who showed that the bottom shear stress is still not entirely in phase with the irrotational velocity at the bottom. However, the magnitude of the negative bottom shear stress is smaller for higher Reynolds number flows. This feature will have a significant influence on sediment transport calculations and the resulting morphological changes. It would be of great interest to perform a set of detailed PIV experiments inside the turbulent boundary layer.

This work was supported by grants from National Science Foundation to Cornell University (OCE-0452862 and CTS-0427115). Yong Sung Park would also like to acknowledge the support from Korea Science and Engineering Foundation under grant number M06-2004-000-10541-0.

REFERENCES

Chang, K.-A. & Liu, P. L.-F. 1998 Velocity, acceleration and vertical vortex under a breaking wave. *Phys. Fluids* **10**, 327–329.

Chang, K.-A. & Liu, P. L.-F. 1999 Experimental investigation of turbulence generated by breaking waves in water of intermediate depth. *Phys. Fluids* **11**, 3390–3400.

Cowen, E. A. & Monismith, S. G. 1997 A hybrid digital particle tracking velocimetry technique. *Exps. Fluids* **22**, 199–211.

Cowen, E. A., Sou, I. M., Liu, P. L.-F. & Raubenheimer, B. 2003 Particle image velocimetry measurements within a laboratory-generated swash zone. *J. Engng Mech.* **129**, 1119–1129.

Goring, D. K. 1978 Tsunamis – The propagation of long waves onto a shelf. *Rep.* KH-R-9. W. M. Keck Laboratory of Hydraulics and Water Resources, California Institute of Technology.

Grimshaw, R. 1971 The solitary wave in water of variable depth. Part 2. *J. Fluid Mech.* **46**, 611–622.

Ippen, A. T. & Mitchell, M. M. 1957 The damping of the solitary wave from boundary shear measurements. *Tech. Rep., Hydrodynamics Laboratory* 23. Massachusetts Institute of Technology.

Jensen, B. L., Sumer, B. M. & Fredsoe, J. 1989 Turbulent oscillatory boundary layers at high Reynolds numbers. *J. Fluid Mech.* **206**, 265–297.

Keulegan, G. H. 1948 Gradual damping of solitary wave. *J. Res. Natl Bur. Stand.* **40**, 607–614.

Lin, J. C. & Rockwell, D. 1994 Instantaneous structure of a breaking wave. *Phys. Fluids* **6**, 2877–2879.

Lin, J. C. & Rockwell, D. 1995 Evolution of a quasi-steady breaking wave. *J. Fluid Mech.* **302**, 29–43.

Liu, P. L.-F. 2006 Turbulent boundary-layer effects on transient wave propagation in shallow water. *Proc. R. Soc. Lond.* A **462**, 3431–3491.

Liu, P. L.-F., Al-Banna, K. A. & Cowen, E. A. 2004 Water wave induced boundary layer flows above a rippled bed. In *Advances in Coastal and Ocean Engineering: PIV and Water Waves* (ed. J. Grue, P. L.-F. Liu & G. K. Pedersen), vol. 9, pp. 81–117. World Scientific.

Liu, P. L.-F., Davis, M. H. & Downing, S. 1996 Wave-induced boundary layer flows above and in a permeable bed. *J. Fluid Mech.* **325**, 195–218.

Liu, P. L.-F. & Orfila A. 2004 Viscous effects on transient long-wave propagation. *J. Fluid Mech.* **520**, 83–92.

Liu, P. L.-F., Simarro, G., VanDever, J. & Orfila, A. 2006 Experimental and numerical investigation of viscous effects on solitary wave propagation in a wave tank. *Coastal Engng* **53 (2/3)**, 181–190.

Mei, C. C. 1983 *The Applied Dynamics of Ocean Surface Waves.* John Wiley & Sons.

Mei, C. C. & Liu, P. L.-F. 1973 The damping of surface gravity waves in a bounded liquid. *J. Fluid Mech.* **59**, 239–256.

Ott, E. & Sudan, R. N. 1970 Damping of solitary waves. *Phys. Fluids* **13**, 1432.

Russell, J. S. 1838 Report of the Committee on Waves. *Rep. Meet. 7th Brit. Assoc. Adv. Sci., Liverpool, 1837*, pp. 417–496. John Murray, London,

Sleath, J. F. A. 1987 Turbulent oscillatory flow over rough beds. *J. Fluid Mech.* **182**, 369–409.